ISSN 0021-3640, JETP Letters, 2016, Vol. 104, No. 5, pp. 323–328. © Pleiades Publishing, Inc., 2016.

CONDENSED MATTER

Transport of Electrons on Liquid Helium in a Microchannel Device near the Current Threshold[1]

N. R. Beysengulov[a, b, *], D. G. Rees[b, c], D. A. Tayurskii[a, b], and K. Kono[a–c]

[a] *KFU–RIKEN Joint Research Laboratory, Institute of Physics, Kazan Federal University, Kazan, 420008 Russia*

[b] *RIKEN CEMS, 351-0198 Wako, Japan*

[c] *NCTU–RIKEN Joint Research Laboratory, Institute of Physics, National Chiao Tung University, 300 Hsinchu, Republic of China*

**e-mail: n.beysengulov@gmail.com*

Received July 25, 2016

We study the transport of strongly interacting electrons on the surface of liquid helium confined in a microchannel geometry, near the current threshold point. The current threshold depends on the electrostatic confinement, created by the microchannel electrodes, and on the electrostatic potential of electron system. Depending on the geometry of the microchannel, the current pinch-off can occur at the center or move to the edges of the microchannel, as confirmed by Finite Element Model calculations. The confining potential dependence of electron conductivity above the current threshold point is consistent with a classical charge continuum model. However, we find that below the threshold point electron transport is suppressed due to charging energy effects.

DOI: 10.1134/S002136401617001X

Surface-state electrons (SSE) trapped on the surface of liquid helium represent the simplest example of a strongly interacting Coulomb system [1, 2]. Polarization of the dielectric liquid by the elementary charge induces an attractive force towards the liquid surface. However, at the helium surface a high potential barrier (~1 eV) prevents the electron entering the liquid. In the resulting potential well, the electron motion perpendicular to the surface is quantized and, at low temperatures, electrons occupy only the ground level. Due to its inherent low density, the 2D electron system trapped at the liquid surface is nondegenerate, and because the permittivity of liquid helium is close to that of vacuum, the Coulomb interaction between the electrons is essentially unscreened. In addition, the helium surface has no defects and is perfectly clean. By changing the pressing field $E_\perp$, the SSE density, and so the ratio of Coulomb energy to the thermal energy of electrons can be controlled. This allows the observation of a transition to an ordered state known as the Wigner Solid [3, 4].

The SSE density range ~10^8–10^9 cm^{-2} gives a typical interelectron separation of 0.5–1 μm. Such length scales are accessible using modern nanofabrication techniques. This has led to an increased activity in investigations of the properties of small ensembles of SSE in microstructured devices, the sizes of which can be made comparable with interelectron distance. Generally, geometrical confinement results in an enhancement of correlated electron behavior in low-dimensional systems [5]. For SSE, transport measurements in point-contact devices show the appearance of conductance plateau, attributed to the changing of the number of electrons that can simultaneously pass through the constriction [6, 7]. In addition, commensurability dependent reentrant melting behavior has been demonstrated in quasi-one-dimensional (q1D) SSE systems, formed in long microchannels filled with liquid helium [8–10]. For both types of microdevices, single-electron transport was demonstrated close to the current threshold point [6, 11]. Strong electrostatic confinement, comparable in strength with Coulomb interactions in the SSE system, is essential to observe these effects. However, the influence of electrostatic confinement on the electron transport close to the threshold point remains only partially understood. Here we present transport measurements of q1D SSE in microchannel devices close to the conductance threshold point. Finite Element Modelling (FEM) is used to calculate the electrostatic confinement effects, allowing a quantitative understanding of the SSE transport behavior.

Two devices S1 and S2 were prepared using standard UV-lithography techniques. The details of the device fabrication are described elsewhere [12, 13].

[1] The article is published in the original.

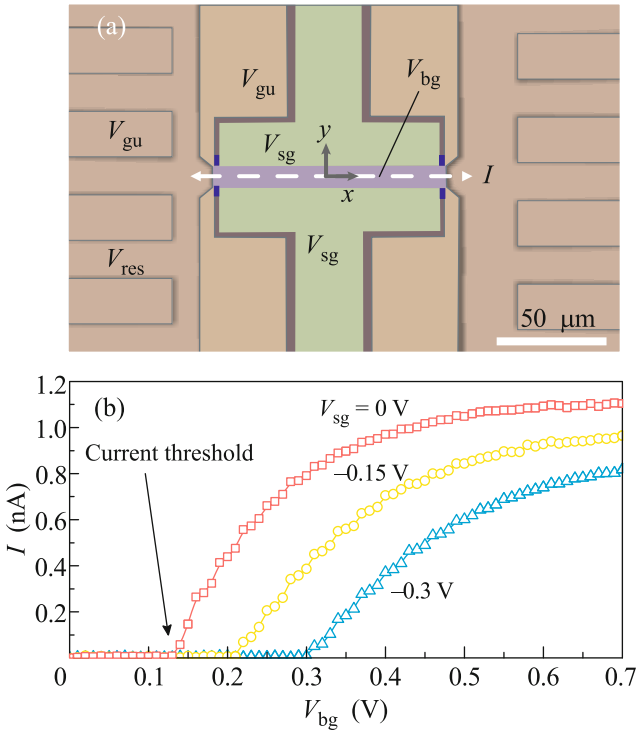

Fig. 1. (Color online) (a) Optical microscope image of the device S1 used for SSE transport measurements. A similar device was used in [12]. The dashed horizontal arrow indicates the direction of the electron motion (and measured electric current). (b) Characteristic electric current I versus V_{bg} at three different V_{sg} values for the sample S1. Here, $T = 1.3$ K, $V_{ac} = 2.1$ mV.

Figure 1a shows an image of the central area of the device. The device consists of two sets of microchannel arrays, which are used as SSE reservoirs. The microchannels are formed by a 100 nm-thick bottom Reservoir Electrode and top Guard electrodes made from Au, separated by insulating hard-baked photoresist. The two reservoirs are connected by a smaller 100 μm-long central microchannel (CM). The CM is formed by Split Gate (SG) and Bottom Gate (BG) electrodes, with channel width $W = 7$ (10) μm and depth $d = 1.9$ (1.6) μm for the device S1 (S2). The lateral electrostatic confinement in the CM is formed by applying V_{bg} and V_{sg} voltages on BG and SG electrodes, respectively. Voltages V_{res} and V_{gu} are applied to the Reservoir and Guard electrodes, respectively, to hold electrons in the reservoirs. The microchannels are filled with superfluid ^{4}He by capillary action. SSE are generated by thermionic emission from a tungsten filament placed above the device. A modulation of the voltage on the Left Reservoir electrode with an ac-signal of small amplitude V_{ac} and frequency $f = 201$ kHz induces a charge flow between the reservoirs. The electric current induced in the Right Reservoir electrode I is detected using standard ac lock-in techniques. The circuit is well described by a lumped-circuit RC model [14].

To understand our data quantitatively, we use a simple electrostatic model of the system. The SSE within the CM are treated as a charge continuum with electrostatic potential ϕ_e. FEM is implemented to calculate the average areal density n_s, the linear density n_l, the effective width of the charge sheet in the channel w_e, and the shape of the electrostatic confinement $\phi(y)$ [15, 16]. The number of electron rows is defined by $N_y = \sqrt{n_l w_e}$. The value of ϕ_e is determined by the electrostatic potential of electrons in the reservoirs, as the reservoir area is much larger than that of the CM. The shape of the electrostatic confinement close to the center of the CM is well described by a parabola $\phi(x = 0, y) \approx \phi_0 - aV_{conf}y^2$, where $a = 2.5(1.1) \times 10^{10}$ m^{-2} for device S1 (S2), $V_{conf} = V_{bg} - V_{sg}$ is confinement parameter, and $\phi_0 = \alpha V_{bg} + \beta V_{sg}$, with the coupling constants α and β satisfying the condition $\alpha + \beta = 1$. The characteristic harmonic frequency related to the lateral confinement is $\omega = \sqrt{2a(V_{bg} - V_{sg})e/m_e} \simeq 10^{11}$ rad s^{-1} at the typical experimental value of $V_{bg} - V_{sg} = 1$ V (here, e and m_e are the elementary charge and bare electron mass, respectively). Note that for the nondegenerate SSE system we do not expect conductance quantization as observed for degenerate Fermi gases in quantum point-contact devices [6].

Figure 1b shows the electric current I versus V_{bg} at temperature $T = 1.3$ K and constant $V_{sg} = 0$ V for device S1. An increase in the current above a threshold value of V_{bg} is observed as V_{bg} is swept positive. According to our electrostatic model, electrons are unable to move through the CM when the electrostatic potential at the channel center ϕ_0 becomes more negative than ϕ_e. Above the threshold value, electrons enter the CM and, on increasing V_{bg} further, the number of charge carriers increases in the CM. This leads to the increase in the measured electric current. On changing V_{sg} to more negative values, the current threshold shifts to the right in Fig. 1b, in accordance with our model.

The threshold points fall close to a single line in the (V_{bg}, V_{sg})-plane, with a slope close to the ratio $-\alpha/\beta$. The values of α and β can be evaluated more directly from the examination of threshold points recorded in experiments where V_{bg} (or V_{sg}) is swept at different values of ϕ_e. This can be realized by keeping the difference between V_{res} and V_{gu} constant whilst changing their potential. For example, on changing V_{gu} and V_{res} simultaneously by 10 mV, ϕ_e changes by the same

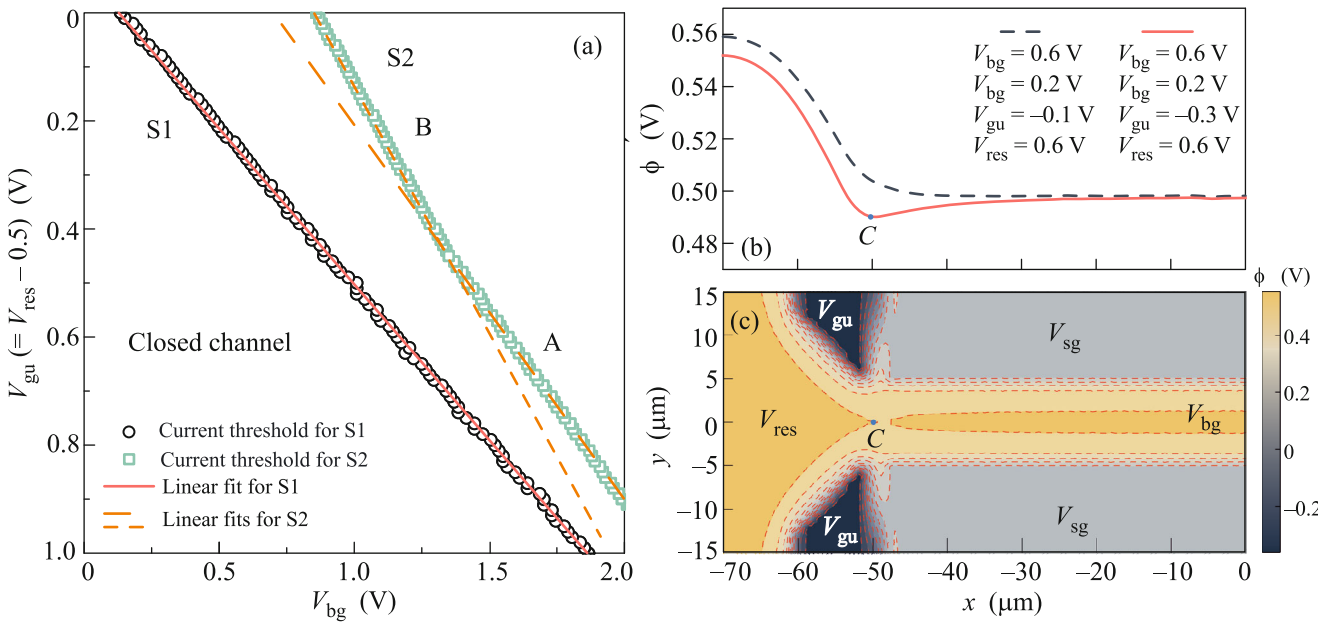

Fig. 2. (Color online) (a) Current threshold points against V_{gu} and V_{bg} for devices S1 and S2. Here, $V_{res} - V_{gu} = 0.5$ V was kept constant and $V_{sg} = 0$ V. The solid line is the linear fit of the data from device S1. Dashed lines represent linear fits for two different regions A and B in data for device S2. (b) Electrostatic potentials $\phi(x, y = 0)$ for two different sets of electrode voltages, corresponding to the different threshold conditions for device S2. Electron transport is allowed when $\phi_e < \min(\phi(x, y = 0))$. (c) The result of FEM modelling of $\varphi(x, y)$ along the liquid helium surface for S2 with $V_{bg} = 0.6$ V, $V_{sg} = 0.2$ V, $V_{gu} = -0.3$ V, and $V_{res} = 0.6$ V.

amount. Threshold points on the (V_{bg}, V_{gu})-plane for samples S1 and S2, measured with $V_{res} - V_{gu} = 0.5$ V, are presented in Fig. 2a.

For device S1, the points form a line with slope ≈ 0.59 (see Fig. 2a), which is close to the value $\alpha = 0.61$ obtained from FEM calculations.

The behavior of the threshold points is different for the device S2. Figure 2a shows two distinct lines with different slopes. The current threshold points for $V_{gu} > 0.5$ V follow the slope 0.72. For $V_{gu} < 0.5$ V the threshold points follow a different line with slope 0.95. Examination of the electrostatic potential map across the device reveals that the minimum of $\phi(x, y = 0)$ usually appears at the center of CM. In this case, the threshold points are defined for the point $x = 0$ (dashed line in Fig. 2b). FEM calculations at the center of CM give $\alpha = 0.75$, which is consistent with the experimental data for $V_{gu} > 0.5$ V. However, under some conditions, the minimum of $\phi(x, y = 0)$ shifts to the edges of the CM (point C) as shown in Figs. 2b, 2c, where the influence from the other electrodes modifies the coupling constants α and β. Consequently, the slope of the threshold line changes. The examination of the threshold conditions from FEM yields the slope defined as $\alpha/(1 - \gamma - \delta) = 0.89$, which demonstrates a good agreement with experimental data for $V_{gu} < 0.5$ V. Here, γ and δ are coupling constants of GU and RES electrodes, respectively. Note that for the device S1 FEM analysis shows that the potential minima always occurs at $x = 0$. The difference between devices S1 and S2 is determined by the difference in the geometry of the electrodes near CM area. This analysis demonstrates a good understanding of the threshold condition and the electrostatic profile of the devices.

In Fig. 3a, the electric current I versus V_{sg} is shown at different values of V_{bg} for device S1. I varies smoothly above the current threshold $V_{sg} > V_{sg}^{th}$, as predicted by the charge continuum model. However, an abrupt drop of the current signal occurs at the threshold point that is not consistent with this model. Here, at the current threshold, the charge continuum model is expected to break down due to extremely low electron densities. The observed signal jump can be considered a consequence of the granular nature of charges. In this case, transport through the CM is allowed when the charging energy of the CM area is overcome.

The charging energy is given by $E_C = e^2/2C$. The question here, however, is what capacitance should be employed. A naive guess may be to employ a capacitance associated with the whole channel, which is expressed as $C = \varepsilon\varepsilon_0 S/d$ under a simple capacitor

approximation, where $S = w_e \times L$ and $L \simeq 100$ μm is the length of channel, $w_e = 1$ μm, a value which is typically obtained in our experiment, ε and ε_0 are the dielectric constant of liquid ^{4}He and vacuum permittivity, respectively. This capacitance gives a charging energy of $E_C \approx e \times 0.17$ mV, which is too small to explain the observed jump. However, if we consider a square area determined by effective width of the CM, which defines the capacitance, then $S = w_e^2$. Here we estimate charging energy $E_C \approx e \times 17$ mV. The charging energy is much larger than k_BT for typical experimental conditions, which should be stable enough to be observed, where k_B is the Boltzmann constant. Consequently, charge transport is favored when $\alpha V_{bg} + \beta V_{sg} \geq \varphi_e + 2E_C/e$.

In a quantum-mechanical picture, the monochromatic electron wavefunction is a plane wave, and spatially extended. However, because the channel length is much larger than the thermal de Broglie wavelength of the electron, we consider that a single electron cannot occupy the whole channel simultaneously. Therefore, we attribute our observation of current jump at the threshold point to the charging energy, which is determined at the entrance of the CM rather than the entire channel area.

This simple granular charge model has several important consequences. Firstly, once the threshold is exceeded, electrons continue to enter the channel until the electron-electron distance becomes comparable to w_e. This is observed in the experiment as a finite current jump at the threshold point I_{th} (see Fig. 3a).

A single chain of electrons is formed at the current threshold point with a finite linear density defined by the effective width of the channel, $n_l = 1/w_e$. With decreasing V_{conf} the amplitude of the current jump I_{th} increases. By changing V_{bg}, the pressing electric field experienced by the electrons also changes: $E_\perp = (\phi_e - V_{bg})/d$. The mobility of electrons on liquid helium $\mu \sim 1/E_\perp^2$ [1]. The amplitude of the electric current at the threshold is $I_{th} \propto n_l\mu$, where μ depends more strongly on V_{bg} than n_l. Therefore, by decreasing V_{bg} the value of I_{th} tends to increase, as indicated by the dashed line in Fig. 3a.

Secondly, the charging energy should depend on the effective width $w_e(\omega, \phi_e)$, which in turn depends on V_{bg}, V_{sg}, and ϕ_e. ϕ_e can be found by extrapolating the linear part of the current dependence to zero, which gives $\phi_e = \phi_0 = \alpha V_{bg} + \beta V_{sg}^0$. In Fig. 3b the measured $\Delta V_{sg} = V_{sg}^{th} - V_{sg}^0$ at different electrostatic confinement parameters V_{conf} is shown. From the granular

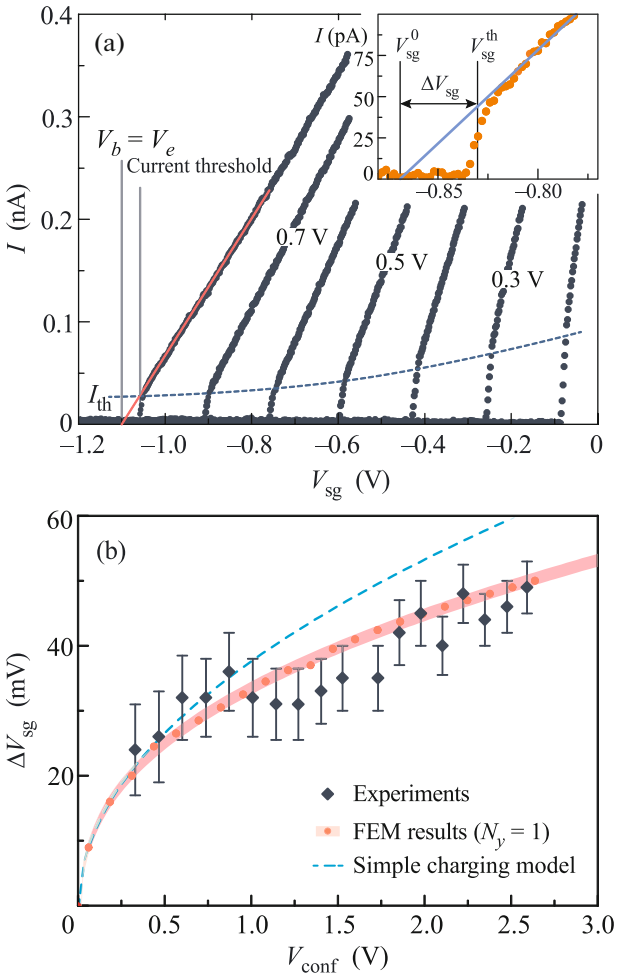

Fig. 3. (Color online) (a) I versus V_{sg} at different V_{bg} values recorded at $T = 1.3$ K for device S1. The dashed line is guide to the eye that indicates the evolution of I_{th}. The inset shows the magnified $I(V_{sg})$ for $V_{bg} = 0.65$ V. Solid lines are the extrapolation of the linear regions of $I(V_{sg})$, which allows V_{sg}^0 to be estimated. (b) Charging voltage ΔV_{sg} versus the confinement parameter V_{conf}. Solid circles are FEM calculation results of $N_y = 1$. The prediction from the charging model is represented by the dashed line.

charge model, we can express the charging voltage ΔV_{sg} as

$$\Delta V_{sg} = \frac{1}{\beta}\sqrt{\frac{ed}{\varepsilon\varepsilon_0}\frac{a}{4}V_{conf}}. \quad (1)$$

The observed increase in ΔV_{sg} with increasing confinement strength is consistent with the charging energy model (see dashed line in Fig. 3b) at small values of the confinement strength. As mentioned above, a single chain of electrons is formed at the threshold point. This corresponds to the condition $N_y = 1$ in the charge continuum model. Therefore, the transport of

electrons through the CM is prohibited when $N_y < 1$. Estimates of ΔV_{sg} from the FEM calculations, which satisfy the condition $N_y(V_{bg}, V_{sg}, \varphi_0) = 1$, are shown by circles in Fig. 3b. These points show better agreement with the experimental data than the values calculated using Eq. (1), because the FEM calculation gives a more accurate estimate of the conditions for which $N_y = 1$. This general agreement supports our interpretation of the data in terms of charging energy effects.

The above-mentioned current jump was observed in the $I(V_{sg})$ dependence, but not in the $I(V_{bg})$ dependence (see Fig. 1b). This is because $\beta < \alpha$, and so the charging voltage $\Delta V_{bg} < \Delta V_{sg}$. The value V_{bg}^0 is difficult to extract from the $I(V_{bg})$ experimental data. The linear $I(V_{sg})$ dependence above the threshold point is due to the constant $E_\perp$ along the V_{sg} sweep, which is in contrast with $I(V_{bg})$ dependence.

The observation of this classical charging effect for a single electron chain is quite unique. We are not aware of any other examples of this effect. We are able to observe it here due to the nondegenerate and strongly interacting nature of the electron system. In addition, the helium substrate is perfectly clean and so transport measurements can be performed at extremely low electron densities. This is in contrast with low-dimensional systems in solid state devices for which pinning by impurities typically restricts transport measurements when the electron density is low. In addition, the charging energy of the SSE system in the CM is large due to its isolation from the environment.

The transport behavior observed in our experiments is in contrast with the transport of degenerate electron gases in quantum point-contact (QPC) devices and nanowires. There the transverse confinement in the QPC and nanowires result in the formation of one-dimensional modes inside the constriction, and the conductance rises in quantized in units of $2e^2/h$ as each subband is populated [17–19]. It is also interesting to compare our results with Coulomb blockade devices in which the observation of peaks in the differential conductance is a demonstration of a single electron transport. This effect is observed in a wide range of mesoscopic conductors such as quantum dots [20], nanowires [21], carbon nanotubes [22, 23], and etc. For nondegenerate electrons on helium, transport through a microscopic constriction shows step-like features in conductance [6], which are different in origin with those observed in QPCs and analogous to the Coulomb blockade effect; the mutual repulsion between electrons restricts the number of charges that can simultaneously pass through the constriction. The device can be therefore be viewed as a classical analog of the QPC. The long microchannel devices investigated here can be viewed as many point-contacts connected in a series, and so a step-like increase in conductance might be expected. However, the larger resistance of the long channel dominates over Coulomb blockade effects that might arise at the channel entrance, and the conductance therefore varies smoothly. The current jump observed at the threshold, when the single chain of electrons is formed in CM, is governed by a classical charging effect.

In conclusion, we have investigated the transport of a classical electron system on liquid helium in a microchannel close to the current threshold point. Above the current threshold point, the SSE transport can be understood in terms of a charge continuum model. However, the observation of a current jump at the current threshold reflects the granular nature of the charges, for which charging energy effects become important. The understanding of electron transport and single-electron control at small length scales is important for the development of quantum information processing schemes with SSE, and for future experimental studies of interacting low-dimensional systems.

We thank A.D. Chepelianskii and Yu. Lysogorskiy for useful discussions. This work was supported by the Japan Society for the Promotion of Science (JSPS, KAKENHI Grant Number JP24000007) and by the Russian Government Program of Competitive Growth of Kazan Federal University. D.G. Rees was supported by the Taiwan Ministry of Science and Technology (MOST, grant nos. MOST 103-2112-M-009-001 and MOST 104-2112-M-009-022-MY3).

REFERENCES

1. E. Y. Andrei, *Two-Dimensional Electron Systems on Helium and Other Cryogenic Substrates* (Kluwer Academic, Dordrecht, 1997).
2. Yu. P. Monarkha and K. Kono, *Two-Dimensional Coulomb Liquids and Solids* (Springer, Berlin, 2004).
3. V. V. Deshpande, M. Bockrath, L. I. Glazman, and A. Yacoby, Nature **464** (7286), 209 (2010).
4. D. G. Rees, I. Kuroda, C. A. Marrache-Kikuchi, M. Höfer, P. Leiderer, and K. Kono, Phys. Rev. Lett. **106**, 026803 (2011).
5. D. G. Rees, H. Totsuji, and K. Kono, Phys. Rev. Lett. **108**, 176801 (2012).
6. H. Ikegami, H. Akimoto, D. G. Rees, and K. Kono, Phys. Rev. Lett. **109**, 236802 (2012).
7. D. G. Rees, H. Ikegami, and K. Kono, J. Phys. Soc Jpn. **82**, 124602 (2013).
8. D. G. Rees, N. R. Beysengulov, J.-J. Lin, and K. Kono, Phys. Rev. Lett. **116**, 206801 (2016).
9. D. G. Rees, I. Kuroda, C. A. Marrache-Kikuchi, M. Höfer, P. Leiderer, and K. Kono, J. Low Temp. Phys. **166**, 107 (2012).
10. Y. Iye, J. Low Temp. Phys. **40**, 441 (1980).
11. N. R. Beysengulov, D. G. Rees, Y. Lysogorskiy, N. K. Galiullin, A. S. Vazjukov, D. A. Tayurskii, and K. Kono, J. Low Temp. Phys. **182**, 28 (2016).

12. F. Hecht, J. Numer. Math. **20**, 251 (2012).
13. D. G. Rees, I. Kuroda, C. A. Marrache-Kikuchi, M. Hofer, P. Leiderer, and K. Kono, J. Low Temp. Phys. **166**, 107 (2012).
14. Y. Iye, J. Low Temp. Phys. **40**, 441 (1980).
15. N. R. Beysengulov, D. G. Rees, Y. Lysogorskiy, N. K. Galiullin, A. S. Vazjukov, D. A. Tayurskii, and K. Kono, J. Low Temp. Phys. **182**, 28 (2016).
16. F. Hecht, J. Numer. Math. **20**, 251 (2012).
17. B. J. van Wees, H. van Houten, C. W. J. Beenakker, J. Gr. Williamson, L. P. Kouwenhoven, D. van der Marel, and C. T. Foxon, Phys. Rev. Lett. **60**, 848 (1988).
18. B. Brun, F. Martins, S. Faniel, B. Hackens, A. Cavanna, C. Ulysse, A. Ouerghi, U. Gennser, D. Mailly, P. Simon, S. Huant, V. Bayot, M. Sanquer, and H. Sellier, Phys. Rev. Lett. **116**, 136801 (2016).
19. J. Kammhuber, M. C. Cassidy, H. Zhang, O. Gul, F. Pei, M. W. A. de Moor, B. Nijholt, K. Watanabe, T. Taniguchi, D. Car, S. R. Plissard, E. P. A. M. Bakkers, and L. P. Kouwenhoven, Nano Lett. **16**, 3482 (2016).
20. L. P. Kouwenhoven, N. C. van der Vaart, A. T. Johnson, W. Kool, C. J. P. M. Harmans, J. G. Williamson, A. A. M. Staring, and C. T. Foxon, Z. Phys. B **85**, 367 (1991).
21. A. Tilke, R. H. Blick, H. Lorenz, J. P. Kotthaus, and D. A. Wharam, Appl. Phys. Lett. **75**, 3704 (1999).
22. S. Sapmaz, P. Jarillo-Herrero, J. Kong, C. Dekker, L. P. Kouwenhoven, and H. S. J. van der Zant, Phys. Rev. B **71**, 153402 (2005).
23. V. V. Deshpande and M. Bockrath, Nat. Phys. **4**, 314 (2008).